Analysis of Solar-Driven Gasification of Biochar Trickling Through an Interconnected Porous Structure

Michael Kruesi, Zoran R. Jovanovic, and Andreas Haselbacher
Dept. of Mechanical and Process Engineering, ETH Zurich, 8092 Zurich, Switzerland

Aldo Steinfeld
Dept. of Mechanical and Process Engineering, ETH Zurich, 8092 Zurich, Switzerland

Solar Technology Laboratory, Paul Scherrer Institute, 5232 Villigen PSI, Switzerland

DOI 10.1002/aic.14672
Published online November 21, 2014 in Wiley Online Library (wileyonlinelibrary.com)

The efficient transfer of high-temperature solar heat to the reaction site is crucial for the yield and selectivity of the solar-driven gasification of biomass. The performance of a gas-solid trickle-bed reactor constructed from a high thermal conductivity porous ceramic packing has been investigated. Beech char particles were used as the model feedstock. A two-dimensional finite-volume model coupling chemical reaction with conduction, convection, and radiation of heat within the packing was developed and tested against measured temperatures and gasification rates. The sensitivity of the gasification rate and reactor temperatures to variations of the packing's pore diameter, porosity, thermal conductivity, and particle loading was numerically studied. A numerical comparison with a moving bed projected a more uniform temperature distribution and higher gasification rates due to the increased heat transfer via combined radiation and conduction through the trickle bed. © 2014 American Institute of Chemical Engineers *AIChE J*, 61: 867–879, 2015
Keywords: biomass gasification, solar reactor, syngas, gas-solid trickle-bed reactor, finite-volume modeling

Introduction

Steam-based gasification of biomass using concentrated solar energy has the potential of becoming a low-carbon footprint route to transportation fuels from a renewable resource.[1,2] At high temperatures and in the presence of steam, biomass is converted to syngas, a mixture of H_2 and CO, which can be processed into diesel or kerosene (Fischer-Tropsch process) or into methanol and then gasoline (MTG, Mobil). Efficient delivery of high-temperature solar heat to the reaction site is crucial for yield and favorable selectivity of the highly endothermic gasification reactions. The most commonly suggested mode for delivering heat is to indirectly irradiate biomass particles entrained in optically opaque tubes within a residence time range of less than a second.[3–9] This, however, requires impractically high operating temperatures as well as energy-intensive and costly preprocessing of the biomass into particles that are small enough to reach the target temperature and react within the short residence time. Moreover, the heat is transferred to the gas phase mainly by convection from the irradiated particles[10] but their effective surface area, set by the particle volume fraction and size, is generally insufficient for reaching gas temperatures required for a favorable selectivity of gas-phase reactions. Alternative concepts based on packed or moving beds (MBs) allow the use of coarser biomass particles. However, these concepts suffer from significantly reduced overall heat transfer due to high attenuation of the thermal radiation by the densely packed opaque solids.[11,12] As the heat transfer becomes the limiting factor, large temperature gradients and nonuniform reaction rates adversely impact energy conversion efficiency of the solar gasification process.

This work investigates a method for increasing the residence time of the solids and enhancing the heat transfer to the gas phase by incorporating an interconnected reticulate porous ceramic (RPC) structure into a drop-tube reactor. The particles trickle through the RPC and undergo gasification with the concurrently flowing steam. In comparison to the commonly used packings such as spheres, Raschig or Pall rings, cylindrical screens, or regularly stacked structures,[13–18] the RPC has a higher degree of solid connectivity and thus higher effective thermal conductivity at the same porosity. This is of great importance as the process heat is provided externally. Moreover, the structure is less optically dense than a packed or MB hence the radiation penetrates deeper. Finally, by providing a resistance to the flow of solids the structure not only increases the mean residence time of the trickling particles but it also disperses them radially. All these enhancements are expected to provide a more homogeneous radial temperature distribution and decrease the temperature difference between the gas and the solids, thereby increasing reaction yields.

The proposed concept was previously tested for solar gasification of bagasse with steam.[19] In comparison with drop-tube operation it demonstrated both higher carbon conversions and an improved syngas quality. The objective of this work is to understand the mass and heat-transfer phenomena leading to

Correspondence concerning this article should be addressed to Z. R. Jovanovic at zjovanovic@ethz.ch

Table 1. Elemental Analysis of the Beech Char Feedstock

Carbon (C; wt %)	85.94
Hydrogen (H; wt %)	2.50
Oxygen (O; wt %)	8.23
Nitrogen (N; wt %)	0.92
Sulfur (S; wt %)	0.05
Ash (by difference; wt %)	2.36
H/C = x (mol/mol)	0.349
O/C = y (mol/mol)	0.072

the more favorable performance using numerical modeling. For this purpose, a heat transfer model of an allothermal tubular reactor gasifying beech char particles with steam is developed considering steady state, two-dimensional (2-D) finite-volume material, and energy balances. The model accounts for all three modes of heat transfer: conduction and radiation from the wall through the RPC and convection from the RPC surface to the flowing gas. The contribution of the chemical reaction is evaluated based on an apparent first-order rate law after adopting a suitable value of the activation energy from the literature and optimizing the pre-exponential factor for the best agreement between the model predictions and experimental results obtained in a laboratory-scale electrically heated reactor prototype. The model is then used to assess the sensitivity of the gasification rate and the reactor temperatures to the particle loading and the RPC properties such as pore diameter, porosity, and thermal conductivity. In addition, the performance of the trickle-bed reactor was numerically compared to the performance of a MB as an alternative concept for increasing the residence time of the char particles.

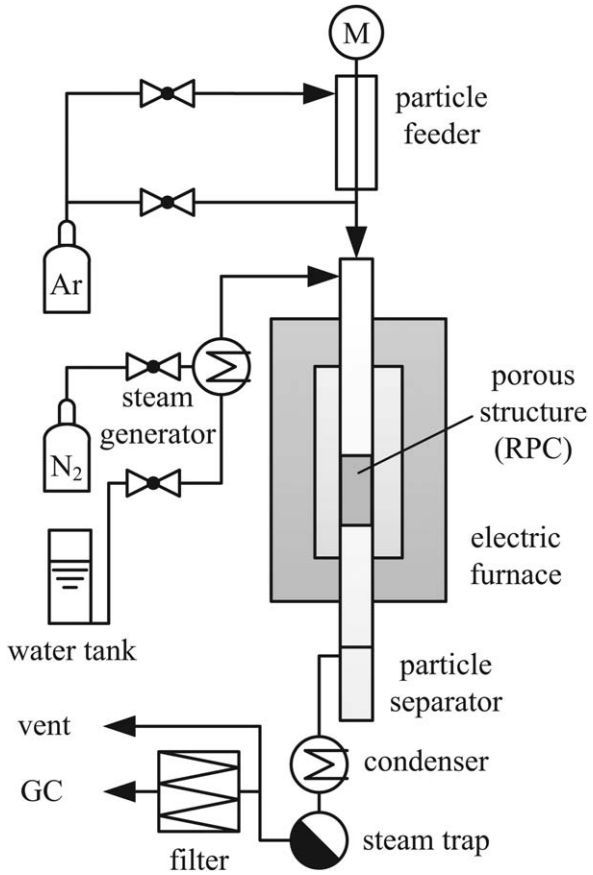

Figure 1. Schematic of the experimental setup.

Methods and Materials

Feedstock

Beech char particles (proFagus GmbH, Bodenfelde, DE) obtained by pyrolysis of raw beech were chosen as model feedstock for this study because they exhibit good flowability and allow investigating the steam gasification reaction without the intrusion by pyrolysis products. Prior to their use in the reaction, the particles were dried (378 K, $>$ 4 h), ground, and sieved to a particle size range of 0.56–1.00 mm with a mean size of 0.81 mm (LA-950 analyzer, HORIBA). The bulk density of the resulting slumped bed of particles was determined to be $\rho_{char,bulk} = 280$ kg/m^3.[20] The elemental analysis (LECO Corporation, St. Joseph, US-MI: CHN-900, RO-478, CHNS-932) implies $CH_{0.349}O_{0.072}$ as the overall char chemical formula after neglecting the presence of ash, N, and S (Table 1). The lower heating value (LHV) has been reported to be 32.13 MJ/kg.[12] The initial ash deformation temperature is expected at around 1773 K.[21,22]

Experimental setup

A schematic of the experimental ambient-pressure concurrent gas-solid trickle-bed reactor setup is shown in Figure 1. A 1.2 m long alumina reactor tube having an inner diameter of 0.06 m and a wall thickness of 5 mm was situated inside an electrical tube furnace (Carbolite) to simulate the conditions of absorbing cavity-receivers that are heated by concentrated solar radiation.[6,19] Two 0.1-m-tall RPC pieces, as the one shown in Figure 2, were stacked and inserted into the alumina tube with the stack's top at the middle of the hot zone and held in place by another smaller diameter supporting alumina tube. The RPC was made of SiSiC (silicon-infiltrated silicon carbide) with a high thermal conductivity ($k_{SiC} = 36$ W/m K at 1273 K) and an overall porosity of $\varphi_{RPC} = 89\%$ with a nominal pore diameter of $d_{nom} = 2.54$ mm corresponding to 10 ppi (pores per inch).

Temperatures were measured with K-type thermocouples located as indicated in Figure 3. C1–C4 and W1–W5

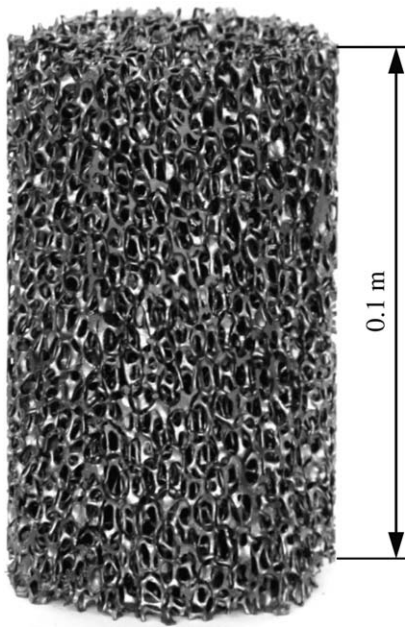

Figure 2. Photograph of the SiSiC reticulate porous ceramic (RPC) with 10 pores per inch (ppi) used as packing in the tubular gasifier.

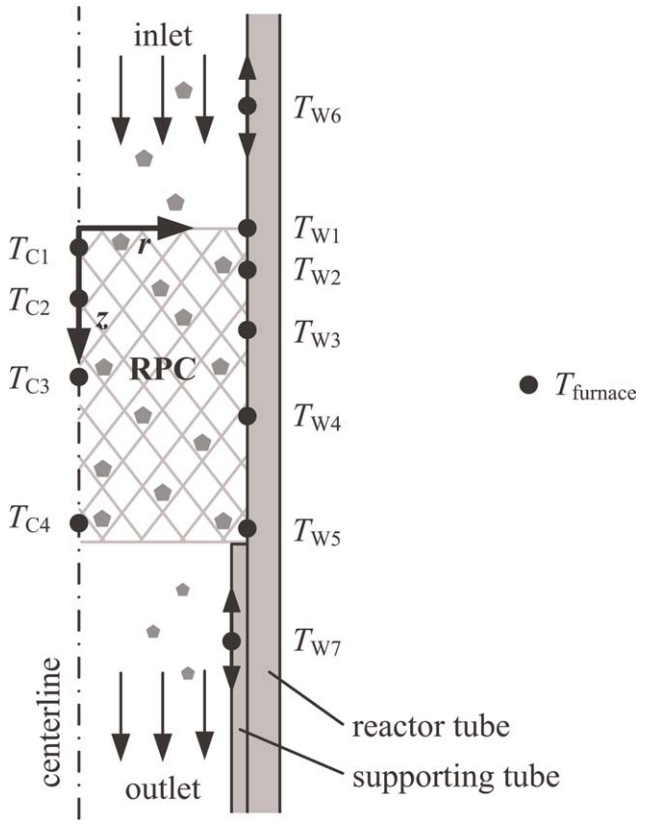

Figure 3. Schematic (not to scale) of the main reactor tube, RPC, and supporting tube assembly indicating thermocouple locations.

Thermocouples T_{W6} and T_{W7} were movable along the tube wall.

measured the temperatures of the RPC along its centerline and the tube/RPC interface, respectively; two additional movable thermocouples W6 and W7 measured the tube temperature above and below the RPC.

The particles were fed via a calibrated feeding system (LAMBDA Laboratory Instruments) from an Ar-purged hopper positioned above the tube. A sweep Ar flow was introduced through a side port below the feeding system to prevent the steam from back-flowing and condensing in the hopper. The N_2-entrained steam generated with an external evaporator (Bronkhorst) was introduced at the top of the alumina tube. The flow rates of the gases and water into the evaporator were controlled with Bronkhorst mass flow controllers pre-calibrated by Bios Definer 220.

Ash and unreacted char were removed from the gaseous product stream in the particle separator located below the reactor just before a condenser and a steam trap. A slip-stream of the product gas was withdrawn after the condenser and analyzed by gas chromatography (GC) after being filtered and chilled to remove particulate matter and condensable components. The two-channel Varian Micro-GC was equipped with Molsieve-5A and Poraplot-U columns ($\sim$1/120 Hz sampling frequency) and was capable of determining concentrations of H_2, N_2, CO, CH_4, CO_2, C_2H_2, C_2H_4, and C_2H_6. The flow rate of N_2 used to entrain the steam was used as reference to calculate the total molar flow rate at the outlet of the reactor.

Experimental procedure

Experiments were completed to test four sets of input conditions: a steam concentration of 15 vol % at nominal furnace temperatures $T_{furnace}$ = 1173, 1223, and 1273 K and a steam concentration of 20 vol % at $T_{furnace}$ = 1223 K. Each experimental condition was tested twice to ensure repeatability. Additionally, a free-fall drop-tube reference experiment with no RPC in place was completed with the inlet steam concentration of 15 vol % at $T_{furnace}$ = 1273 K.

After being purged with Ar and leak-tested, the reactor was preheated to the desired furnace temperature. The flows of Ar, N_2, and water were set to provide a total inlet gas flow rate of 12.12 L_N/min (L_N designates normal liters at 273 K and 1 atm.; 9 mmol/s) to the reactor. After the temperature equilibrated, the biomass feed commenced at a nominal rate of 1.10 g/min corresponding to a mass flux of 6.5 g/s m^2. The resulting molar steam to biomass ratios ($\dot{n}_{H_2O(g)}/\dot{n}_{CH_xO_y}$) were 1.03 or 1.36, corresponding to 1.11 or 1.47 times the stoichiometric amount of steam for the idealized net reaction represented by

$$CH_xO_y + (1-y)H_2O \rightarrow \left(1+\frac{x}{2}-y\right)H_2 + CO \qquad (1)$$

Temporal gas compositions, temperature, and pressure data were recorded over the course of each experiment (43–51 min). The reactor was operated without any interruptions and without clogging of the RPC or increase in pressure drop across the reactor. Ash and char deposited on and below the RPC were easily removed after the experiments and analyzed for carbon content (LECO Corporation, St. Joseph, US-MI: CHN-900).

Experimental results

The temporal flow rates of H_2, CO, CO_2, and CH_4 over the duration of a typical experiment are shown in Figure 4. The concentrations of C_2H_2, C_2H_4, and C_2H_6 were below the detection limit of the GC. After a rapid increase following the introduction of the particles into the hot zone ①, the product flow rates slowly approached asymptotic values toward the end of the experiment ②. The product flow rates were averaged over the final 10 min of each experiment to obtain representative steady-state test conditions.

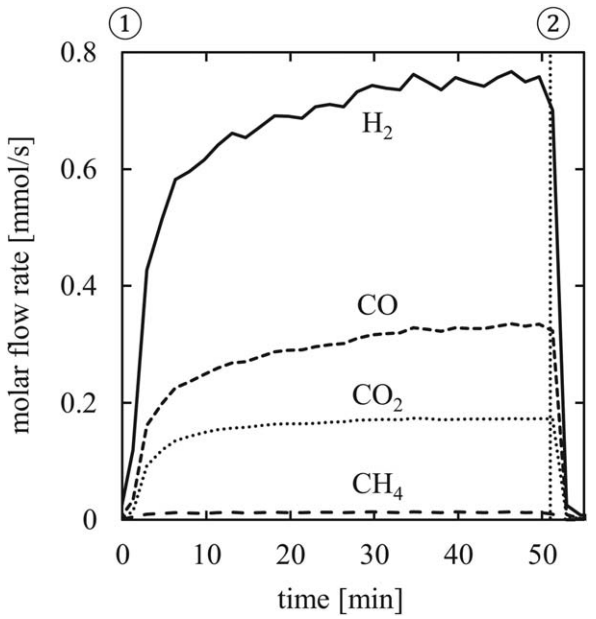

Figure 4. Temporal product gas flow rates over the course of a typical experiment.

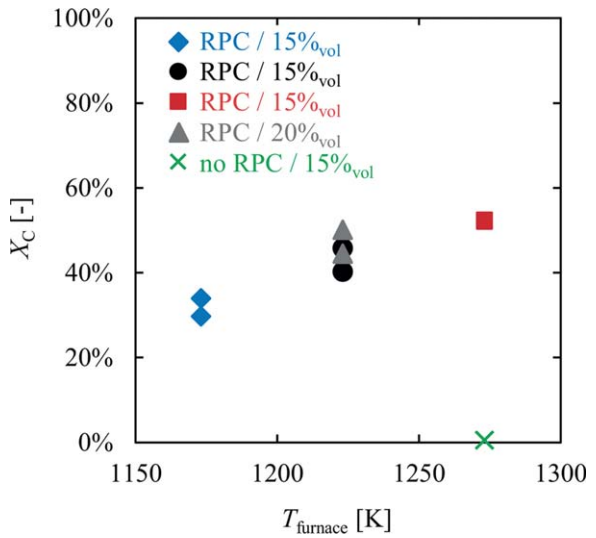

Figure 5. Carbon conversion (X_C) as function of furnace set-point temperature ($T_{furnace}$), steam concentration, and gasifier configuration (RPC versus drop tube).

[Color figure can be viewed in the online issue, which is available at wileyonlinelibrary.com.]

The carbon conversion (X_C) was defined as the average molar flow rate of carbon leaving the reactor with the monitored product gases ($\dot{n}_{C,syngas}$) divided by the average molar flow rate of carbon introduced into the reactor with the char particles ($\dot{n}_{C,char}$), that is

$$X_C = \dot{n}_{C,syngas}/\dot{n}_{C,char} \tag{2}$$

As shown by Figure 5, the carbon conversion in any of the experiments with the RPC was significantly higher than in the reference free-fall drop-tube experiment where the conversion was negligible (less than 1%). Furthermore, the carbon conversion responded well to the furnace temperature: increasing the furnace temperature from 1173 to 1273 K resulted in an increase in carbon conversion from 32% to 52%.

The carbon balance comparing the carbon fed with the carbon in the collected solid products and the product gas could be closed in all experiments within less than 3%. This difference is attributed to the inability to collect all the solids from the filter and the time resolution of the GC sampling (~2 min) that was not sufficient to capture fluctuations in the gas production.

Numerical model

To understand the origin of the experimentally observed enhancing effect of the trickle-bed zone on char gasification, a steady-state 2-D numerical model of the reactor was developed. The model provides information on the spatial variations of temperature, steam concentration, and reaction rate within the trickle bed as well as on the relative contribution of the heat transfer by conduction, convection, and radiation. The model is based on a 2-D axisymmetric finite-volume representation of a domain encompassing the RPC and its pores that are considered to be filled with gas and particles. A 2-D representation is imposed by the fluid flow and heat flux entering the domain in different directions: fluid flow axially from the top and the heat flux radially from the tube wall. The domain is treated as a porous medium with separate solid and fluid phases. The char particles are assigned to the solid phase and gasified according to the overall stoichiometry given by Eq. 1. They are considered spatially isothermal, consistent with the analysis by Weimer and Clough[23] who reported that for the size range considered the conduction within the particles is fast compared to radiation and gas-phase conduction. The mass balance for the solid phase was not solved explicitly. Instead, a constant mass of char per unit volume was assigned to the whole domain. With this simplification, the thermal inertia of the particles amounting to about 10% of its gasification enthalpy is neglected.

Governing equations

The mass balance of the fluid phase is

$$\frac{1}{r}\frac{\partial}{\partial r}(r\rho u_r)+\frac{\partial}{\partial z}\rho u_z=\sum_k S_k \tag{3}$$

where u_z and u_r are the superficial velocities in the axial and radial directions, and ρ is the density of the gas mixture. The mass source terms S_k account for the mass of each species k generated by the chemical reaction.

The fluid-phase conservation equation for species $k = 1, 2,\ldots, N-1$ are given by

$$\frac{1}{r}\frac{\partial}{\partial r}[r\rho(u_r+v_r^C)w_k]+\frac{\partial}{\partial z}[\rho(u_z+v_z^C)w_k] = \frac{1}{r}\frac{\partial}{\partial r}\left(r\rho D_{\mathrm{eff},k,\perp}M_k\bar{M}\frac{\partial y_k}{\partial r}\right)+\frac{\partial}{\partial z}\left(r\rho D_{\mathrm{eff},k,\parallel}M_k\bar{M}\frac{\partial y_k}{\partial z}\right)+S_k \tag{4}$$

where w_k and y_k are the mass and mole fractions of species k, $D_{\mathrm{eff},k,\perp}$ and $D_{\mathrm{eff},k,\parallel}$ are the effective diffusion coefficients within the porous media perpendicular and parallel to the main flow direction, and v_r^C and v_z^C are correction velocities to ensure global mass conservation[24]

$$v_r^C=\sum_k D_{k,\perp}M_k\bar{M}\frac{\partial y_k}{\partial r} \tag{5}$$

$$v_r^C=\sum_k D_{k,\parallel}M_k\bar{M}\frac{\partial y_k}{\partial z} \tag{6}$$

The fluid-phase energy equation based on the sensible internal energy of the fluid e_s can be written as

$$\frac{1}{r}\frac{\partial}{\partial r}(r\rho u,e_s)+\frac{\partial}{\partial z}(\rho u_z e_s)=\frac{1}{r}\frac{\partial}{\partial r}\left[r\rho\sum_k\left(h_{s,k}D_{\mathrm{eff},k,\perp}M_k\bar{M}\frac{\partial y_k}{\partial r}\right)\right] + \frac{\partial}{\partial z}\left[\rho\sum_k\left(h_{s,k}D_{\mathrm{eff},k,\parallel}M_k\bar{M}\frac{\partial y_k}{\partial z}\right)\right]+h_{sf}A_0(T_s-T_f) \tag{7}$$

where T_f and T_s are the temperatures of the fluid and solid phases, respectively, $h_{s,k}$ is the sensible enthalpy, M_k is the molar mass of species k, and $\bar{M}$ is the average molar mass of the fluid. The heat transfer between fluid and solid is expressed by an interfacial heat transfer coefficient h_{sf} with A_0 being the interfacial area between the two phases. Finally, as all the heat consumed by the chemical reaction $\dot{Q}_{react}$ is withdrawn from the solid phase, there is no source term contributing to the fluid-phase energy balance. The terms for fluid-phase heat conduction, viscous dissipation, and pressure

work were neglected because $k_s \gg k_f$, $M^2/Re \ll 1$, and $M^2 \ll 1$, respectively. (M and Re were estimated for N_2 at T_f = 1173 K, u_z = 0.31 m/s, γ = 1.33, d_{tube} = 0.06 m, and $\mu = 4.7 \times 10^{-5}$ Pa s.)

The energy balance for the solid phase is expressed as

$$0=\frac{1}{r}\frac{\partial}{\partial r}\left(rk_{eff}\frac{\partial T_s}{\partial r}\right)+\frac{\partial}{\partial z}\left(k_{eff}\frac{\partial T_s}{\partial z}\right)-h_{sf}A_0(T_s-T_f)-\dot{Q}_{react} \tag{8}$$

where k_{eff} is the effective thermal conductivity. The radiative heat transfer within the RPC, an optically thick medium ($\kappa \gg 1$), is modeled with the Rosseland diffusion approximation.[25] An additional term accounting for the radiative contribution k_{rad} is thus included in the definition of the effective thermal conductivity

$$k_{eff}=k_{cond}+k_{rad} \tag{9}$$

where k_{cond} is the thermal conductivity through the RPC. The heat sink due to the heterogeneous chemical reaction (Eq. 1) is given by

$$\dot{Q}_{react}=\Delta H_R \cdot \frac{x_{C,char}\cdot \rho_{char,bulk}\cdot l}{M_C}\cdot r_C \tag{10}$$

where ΔH_R is the heat of reaction, $x_{C,char}$ the carbon mass fraction of the char, $\rho_{char,bulk}$ the bulk density of the char, l the particle loading, and r_C the reaction rate. The heat of reaction was computed based on the LHV and heat capacity of the char and the enthalpy of the gaseous species. The particle loading was defined as

$$l=\frac{m_{char,domain}/\rho_{char,bulk}}{V_{domain}} \tag{11}$$

where $m_{char,domain}$ is the mass of char in the domain and V_{domain} is the volume of the domain. The reaction rate was represented by a first-order Arrhenius-type rate law given by

$$r_C=-\frac{1}{N_C}\frac{dN_C}{dt}=k_0\exp\left(-\frac{E_A}{RT}\right)p_{H_2O} \tag{12}$$

where r_C is the molar gasification rate of carbon per total number of moles of carbon present (N_C), E_A and k_0 are the apparent activation energy and frequency factor, respectively, R is the gas constant, and p_{H_2o} is the partial pressure of steam. This rate law originates from the standard definition of the gasification rate per surface area of char particles

$$r''_C=-\frac{1}{S_C}\frac{dN_C}{dt}=k''_0\exp\left(-\frac{E_A}{RT}\right)p_{H_2O} \tag{13}$$

and the assumption that the carbon surface area S_C decreases linearly with the conversion[26]

$$S_C=S_{C,0}(1-X_C) \tag{14}$$

Thus, recalling that

$$N_C=N_{C,0}(1-X_C) \tag{15}$$

we have

$$r_C=r''_C\frac{S_C}{N_C}=r''_C\frac{S_{C,0}}{N_{C,0}} \tag{16}$$

and

$$k_0=k''_0\frac{S_{C,0}}{N_{C,0}} \tag{17}$$

The apparent activation energy was set to E_A = 196 kJ/mol, a typical value for wood chars reported in the literature.[27] The pre-exponential factor k_0, however, varies strongly with the feedstock source, size, and morphology. For the purpose of this study, k_0 was set to $3.3\cdot10^6$ $s^{-1}bar^{-1}$, which provided good agreement between the simulated and measured overall gasification rates ($\dot{n}_{C,syngas}$) and RPC temperatures (T_s).

The mass source terms S_k are given by

$$S_k=\psi_k M_k\cdot\frac{x_{C,char}\cdot\rho_{char,bulk}\cdot l}{M_C}\cdot r_C \tag{18}$$

with

$$\psi_k=\begin{Bmatrix} -(1-y) & \text{for } H_2O \\ 1+x/2-y & \text{for } H_2 \\ 1 & \text{for CO} \\ 0 & \text{for } N_2 \\ 0 & \text{for Ar} \end{Bmatrix} \tag{19}$$

The momentum equations were not solved. Instead, a profile for the axial velocity was prescribed. Because the boundary layer of the flow through a porous medium is rather thin, a uniform axial velocity at any cross-section perpendicular to the axis, that is, $u_z(r,z) = u_z(z)$, was considered to be a reasonable assumption. At the operating pressure of 1 bar, the pressure drop across the RPC is small and was thus neglected.

Boundary conditions

On the tube wall, the temperatures of fluid T_f and solid T_s were set by linear interpolation of the measured wall temperatures and the species mass fluxes were set to zero. At the centerline, symmetry boundary conditions were applied for all the conservation equations. The inlet conditions for the fluid were set by the total mass flow rate $\dot{m}_{f,in}$, the fluid temperature $T_{f,in}$, and the inlet mass fractions of the species $w_{k,in}$. At the outlet, that is, at the bottom of the RPC, the diffusive fluxes of mass and energy were set to zero. The net heat fluxes across the inlet and outlet boundaries of the solid phase were computed using the radiosity method for enclosures[25] to account for the radiative heat exchange of the RPC with the reactor tube and tube ends. The tube and RPC surfaces above and below the RPC were each discretized into 100 segments and 64 rings, respectively; the tube ends were considered as single surfaces. Assuming a nonparticipating medium in the void space, opaque-gray-diffuse surfaces, and uniform temperature, flux, and optical properties over each surface element, the radiative fluxes q_i between the N_{surf} = 165 surface elements were determined from the following system of equations

$$\sum_{j=1}^{N_{surf}}\left(\frac{\delta_{ij}}{\varepsilon_j}-F_{i-j}\frac{1-\varepsilon_j}{\varepsilon_j}\right)\cdot q_j=\sum_{j=1}^{N_{surf}}(\delta_{ij}-F_{i-j})\cdot\sigma T_j^4 \quad i=1,2,\ldots,N_{surf} \tag{20}$$

where δ_{kj} is the Kronecker delta, ε_j is the emissivity of surface j, σ is the Stefan–Boltzmann constant, and F_{i-j} are the configuration factors that were determined analytically.[28,29] The temperatures of the tube elements were based on linear interpolation of the experimentally measured temperatures. The emissivities of the top and bottom surfaces of the RPC were set to $\varepsilon_{RPC,eff}$ = 0.82 so that the radiative flux

Table 2. Heat- and Mass-Transfer Property Correlations

Quantity	Symbol	Source
RPC specific surface	A_0	Suter and Haussener,[33] Eq. 14
RPC tortuosity	τ	Suter and Haussener,[33] Table 1
RPC interfacial heat transfer coefficient	h_{sf}	Suter and Haussener,[33] Eq. 17
Binary diffusion coefficients	$\mathscr{D}_{ij}$	Fuller et al.,[34] Eq. 4
Molecular diffusion coefficient	$D_{m,k}$	Fairbanks and Wilke,[35] Eq. 3
Dispersion coefficient	$D_{d,\perp}$ and $D_{d,\parallel}$	Petrasch,[32] Eqs. C.3 and C.4
Extinction coefficient	K	Petrasch,[32] Eq. 4.24
Solid thermal conductivity SiC	k_s	Munro,[36] Eq. 14a
gas viscosity	μ	Yaws[37]
Gas-phase thermal conductivity	k_f	Yaws[37]
Gas enthalpy	h_s	Chase[38]
Gas isobaric heat capacity	C_p	Chase[38]
Heat capacity of the char	$C_{p,char}$	Merrick,[39] Eq. 8

$$q_{i,\mathrm{RPC}}=\varepsilon_{\mathrm{eff,RPC}}\sigma T_{i,RPC}^4 \tag{21}$$

corresponds to the emission of an isotropic scattering participating media with emissivity $\varepsilon_{SiC} = 0.85$[30] at uniform temperature $T_{j,\mathrm{RPC}}$.[31] The emissivity of the alumina wall was set to $\varepsilon_{Al_2O_3} = 0.28$.[30]

Domain properties

The effective transport properties of the RPC such as thermal conductivity, interfacial heat transfer coefficient, and extinction coefficient have been studied with pore-level Monte-Carlo ray-tracing and finite-volume heat-transfer simulations based on tomographic scans.[32,33] An overview of the correlations that were used in the simulations is given in Table 2.[32–39]

The radiative contribution k_{rad} to the effective thermal conductivity k_{eff} (Eq. 9) was defined according to the Rosseland diffusion approximation for a homogeneous gray medium[25] as

$$k_{\mathrm{rad}}=\frac{16}{3K}\sigma T_s^3 \tag{22}$$

where K is the extinction coefficient that has been correlated for porosities $0.85 < \varphi_{eff} < 0.91$ and $d_{nom} = 2.54$ mm (a 10 ppi RPC) as[32]

$$K=\frac{5.5173}{d_{\mathrm{nom}}}(1-\phi_{\mathrm{eff}}) \tag{23}$$

The char particles deposited on the struts of the RPC were accounted for by adjusting the RPC porosity (φ_{RPC}) by the particle loading

$$\phi_{\mathrm{eff}}=\phi_{\mathrm{RPC}}-l \tag{24}$$

The conductive contribution to k_{eff} was based on a combination of parallel and serial slabs.[32] In the present case where $k_s \gg k_f$ the correlation reduces to

$$k_{\mathrm{cond}}=k_s f_{\mathrm{opt}}(1-\phi_{\mathrm{RPC}}) \tag{25}$$

where $f_{opt} = 0.3823$.[32] Conduction through the particles was neglected due to their low thermal conductivity resulting in a small underestimation of the heat transfer at high particle loadings.

The effective diffusion coefficients $D_{\mathrm{eff},k,\perp}$ and $D_{\mathrm{eff},k,\parallel}$ take into account the molecular diffusion through a porous medium and the dispersion induced by the flow through the porous structure

$$D_{\mathrm{eff},k,\perp}=D_{\mathrm{m},k}\phi_{\mathrm{eff}}/\tau^2+D_{\mathrm{d},\perp} \tag{26}$$

$$D_{\mathrm{eff},k,\parallel}=D_{\mathrm{m},k}\phi_{\mathrm{eff}}/\tau^2+D_{\mathrm{d},\parallel} \tag{27}$$

where $D_{m,k}$ is the molecular diffusion coefficient of species k, τ is the tortuosity, and $D_{d,\perp}$ and $D_{d,\parallel}$ are the dispersion coefficients perpendicular and parallel to the main flow direction, respectively.

Numerical implementation

The governing equations were iteratively solved with a cell-centered finite-volume method. The RPC section of the tube, represented as a cylinder having diameter $d_{tube} = 0.06$ m and height $h_{tube} = 0.2$ m was discretized into N_z by N_r cells in the axial and radial directions, respectively. The discretization in the axial direction was uniform with cell

Table 3. Parameters Used in Order Verification Study (All in SI units)

Variable	A_1	A_2	A_3	A_4
ρ	0.1804	0.05	$2.5/r_{max}$	$3.7/z_{max}$
$D_{\mathrm{eff},k,\perp}$, $D_{\mathrm{eff},k,\parallel}$	2.8 e −4	0.8 e −4	$5/r_{max}$	$3/z_{max}$
y_k	0.3	0.2	$0.7/r_{max}$	$0.8/z_{max}$

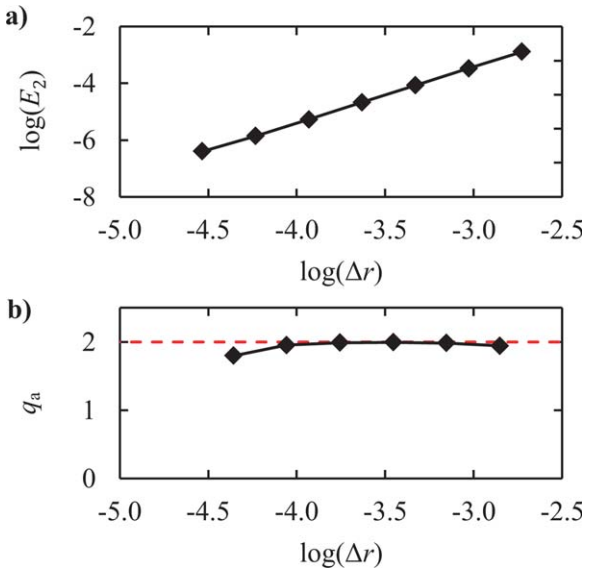

Figure 6. Results from code verification of the diffusion terms in the species equation, (a) error norm E_2 and (b) actual order of accuracy q_a.

[Color figure can be viewed in the online issue, which is available at wileyonlinelibrary.com.]

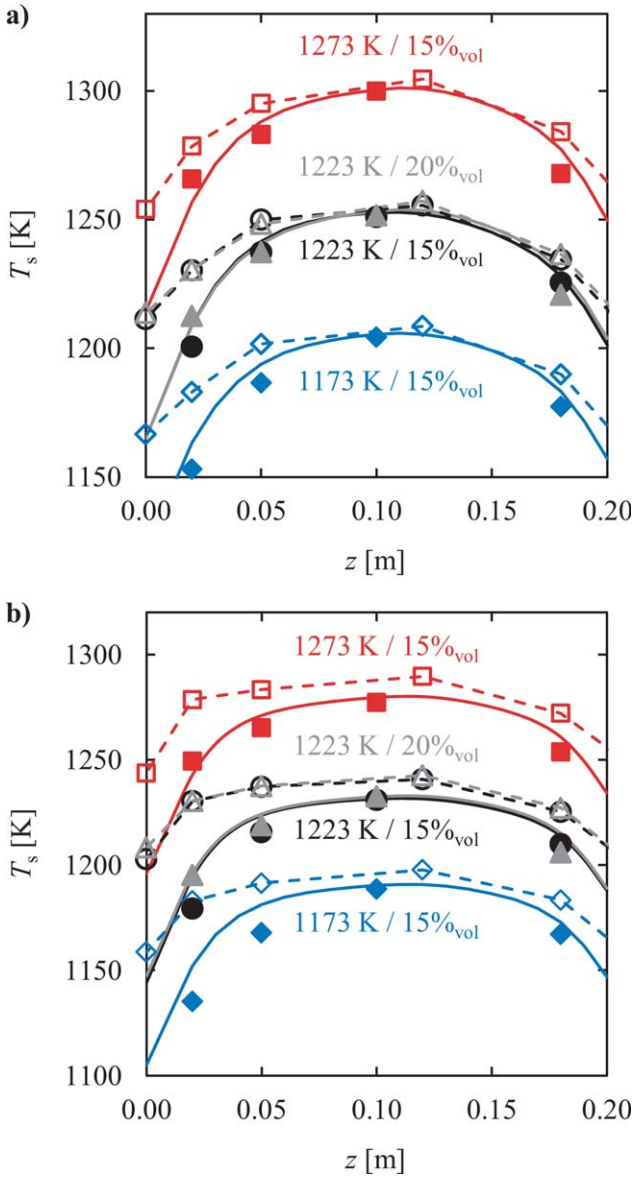

Figure 7. Comparison between experimental ($T_{s,center,exp}$—filled markers) and simulated centerline solid temperature profiles ($T_{s,center,sim}$—solid lines) for (a) nonreacting conditions, and (b) reacting conditions.

The open markers indicate the experimental wall temperatures ($T_{wall,exp}$); the dashed lines represent the boundary temperatures ($T_{wall,bc}$) applied in the simulations. [Color figure can be viewed in the online issue, which is available at wileyonlinelibrary.com.]

heights Δz. In the radial direction, the mesh was refined towards the wall to resolve the large temperature and concentration gradients. The radial cell sizes were given by

$$\Delta r_i = 1.2^{16/N_r} \Delta r_{i+1} \tag{28}$$

The mass balance equation for the fluid phase (Eq. 3) was used to compute the velocity field. After integrating Eq. 3 over each control volume, the resulting equations were summed in the radial direction, thereby eliminating the radial velocity component. In combination with the axial velocity at the domain boundary and the prescribed velocity profile, this allowed sequentially solving for the axial velocity leaving the control volumes at each axial coordinate. Once the axial velocities were known for the whole domain, the integrated mass balance equations could be sequentially solved for the radial velocity in all control volumes.

The governing equations for the $N - 1$ species, the energy of the fluid phase, and the solid energy were discretized using the hybrid scheme[40] and written into individual linear systems. The solutions of the sparse linear systems were found using MATLAB, either by permutation and forward solving or by the unsymmetric-pattern multifrontal method.[41]

At a given iteration step, the velocity field is computed and the species and the fluid and solid phase energy equations are solved sequentially, updating the material properties after each equation. The iteration was terminated if the convergence criterion for the residuals of $R_i < 10^{-7}$ was reached for all dependent variables (u_r, u_z, T_s, w_k, e_s). The residuals R_i were defined as the root mean square error over all cells of the ith iteration normalized by the first iteration.

Code verification

An order-verification study was performed using the method of manufactured solutions (MMS)[42] to ensure that the implemented numerical method solves the governing equations correctly.[43] In the MMS, a solution is first assumed (or "manufactured") and inserted into the governing equations. Unless the manufactured solution happens to be an exact solution of the governing equations, the left- and right-hand sides of the equation will differ. This difference is then added to the right-hand side of the governing equations as a source term to make the manufactured solution an exact solution of the modified governing equations. By solving the modified governing equations numerically, the order of accuracy of the numerical method can be determined even for complicated governing equations that include variable physical properties, for example.

In this study, the manufactured solution was of the form

$$\Phi_{man}(r,z) = A_1 + A_2 \cdot \cos(A_3 \pi r) \cdot \cos(A_4 \pi z) \tag{29}$$

where Φ is a generic dependent variable. Physical properties such as thermal conductivity, density, and diffusion coefficients were represented in the same form as the dependent variable. All governing equations and their individual terms were verified using the MMS. For brevity, only the results of the order verification of the diffusive terms in the species equation are reported. The modified equation reads

$$0 = \frac{1}{r}\frac{\partial}{\partial r}\left(r\rho D_{\text{eff},k,\perp} M_k \bar{M} \frac{\partial y_k}{\partial r}\right) + \frac{\partial}{\partial z}\left(\rho D_{\text{eff},k,\parallel} M_k \bar{M} \frac{\partial y_k}{\partial z}\right) + L_k \tag{30}$$

where L_k is the source term to fulfill the governing equation for the manufactured solution. The coefficients in Eq. 29, the dependent variable, and the properties $D_{\text{eff},k,\perp}$, $D_{\text{eff},k,\parallel}$, and ρ are listed in Table 3. Dirichlet boundary conditions were applied on all boundaries.

Figure 6a shows the evolution of E_2, defined as the L_2-norm of the relative errors in each cell, as a function of the radial mesh spacing. The actual order of accuracy q_a, shown in Figure 6b, was calculated as the slope of E_2 of successive data points. When using the hybrid scheme, the expected order of accuracy depends on the Péclet (Pe) number. For Eq. 30, Pe = 0 and the nominal order of accuracy is 2. In

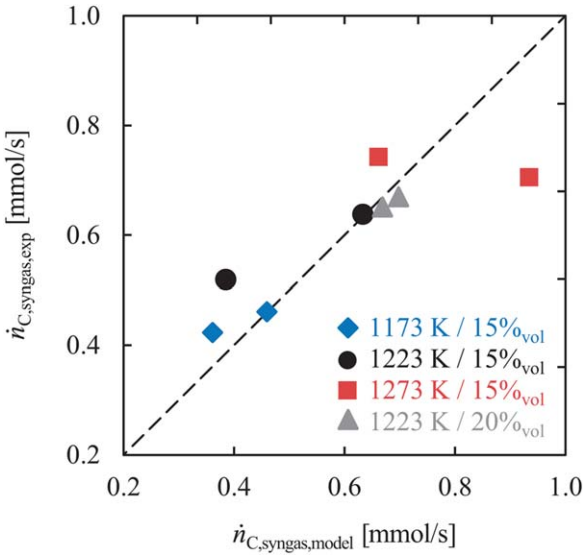

Figure 8. Comparison of experimentally determined and simulated molar flow rates of gasified carbon.

[Color figure can be viewed in the online issue, which is available at wileyonlinelibrary.com.]

the asymptotic range, the actual order of accuracy q_a is very close to the nominal order of accuracy, indicating that the numerical implementation is correct. The numerical implementation of all the other terms in the governing equations was also verified to be correct.

Simulation Results

Model predictions vs. experimental results

The experiments were simulated using a 64 × 64 cell mesh that provided grid-independent solutions. The experimentally determined particle loadings were used as inputs for the simulations of the reactive case. As the fluid temperature at the inlet to the RPC ($T_{f,in}$) was not measured, it was set to the measured wall temperature 0.25 m above the RPC. This was justified by the relative insensitivity of the carbon conversion and the solid temperatures to changes in $T_{f,in}$. (Changing $T_{f,in}$ by ± 100 K influenced the gasification rates by less than 1% and the solid centerline temperature at $z >$ 0.05 m by less than 1 K.)

Figure 7 compares the measured and simulated solid centerline temperatures for the nonreactive (Figure 7a) and the reactive cases (Figure 7b). The open and filled symbols indicate the thermocouple measurements at the wall ($T_{wall,exp}$) and at the centerline ($T_{s,center,exp}$), respectively. The dashed lines indicate the wall temperatures ($T_{wall,bc}$) that were set as boundary conditions in the model. The solid lines are the centerline temperatures ($T_{s,center,sim}$) obtained from the numerical model. The simulations of the nonreactive conditions shown in Figure 7a were used to assess the model performance in terms of heat transfer only. The predicted centerline temperatures are seen to be in good agreement with experimental measurements, thereby indicating the validity of the implemented heat-transfer correlations. Furthermore, the model is capable of predicting the lower centerline temperatures at both upper and lower boundaries of the RPC that reflect the radiation losses to the surroundings. Figure 7b indicates that good agreement between the model and the experiment is also obtained for the reactive cases. The predicted differences between solid and fluid temperatures were in all cases smaller than 1 K for $z > 0.02$ m; larger differences were observed only in the first rows of cells close to the inlet ($z < 0.02$ m).

The parity plot in Figure 8 indicates reasonably good agreement between the simulated and experimentally determined molar flow rates of gasified carbon ($\dot{n}_{C,syngas}$) leaving the reactor. The scatter of the model results for a given furnace temperature and steam concentration are due to differences in the experimentally determined particle loadings.

Sensitivity analysis

Having demonstrated good agreement with the experimental data, the numerical model was used to conduct a sensitivity analysis of the reactor performance with respect to the reactor wall temperature, particle loading, and RPC properties. The analysis was based on a 1 m tall/0.06 m inner-diameter domain that is considered a reasonable scale for a pilot-scale reactor on a solar tower. The simulations were carried out on a grid with 64 and 128 cells in radial and axial direction, respectively, yielding grid-independent solutions for the extended domain.

Simulations performed with uniform wall temperatures of T_{wall} = 1173, 1223, and 1273 K, a particle loading of l = 0.2, and pure steam entering the domain at $\dot{m}_{f,in}$ = 2 g/s and $T_{f,in}$ = 873 K were adopted as reference conditions. The reference conditions were chosen to provide excess steam for all gasification conditions, that is, the maximum steam utilization was around 50%. As the key performance indicators reflecting the reactor productivity and syngas quality, the molar flow rates of the gasified carbon leaving the trickle

Table 4. Simulation Results for a 1 m Tall/0.06 m Inner Diameter Domain with d_{nom} = 2.54 mm, $k_s = k_{SiC}$, φ_{RPC} = 89%, $\dot{m}_{f,in}$ = 2 g/s, $T_{f,in}$ = 873 K, and l = 0.2

Wall temperature T_{wall} (K)	Overall gasification rate $\dot{n}_{C,syngas,RPC}$ (mmol/s)	Centerline temperature at outlet $T_{s,center,outlet}$ (K)
1173	27.0	1099
1223	42.0	1120
1273	58.9	1140

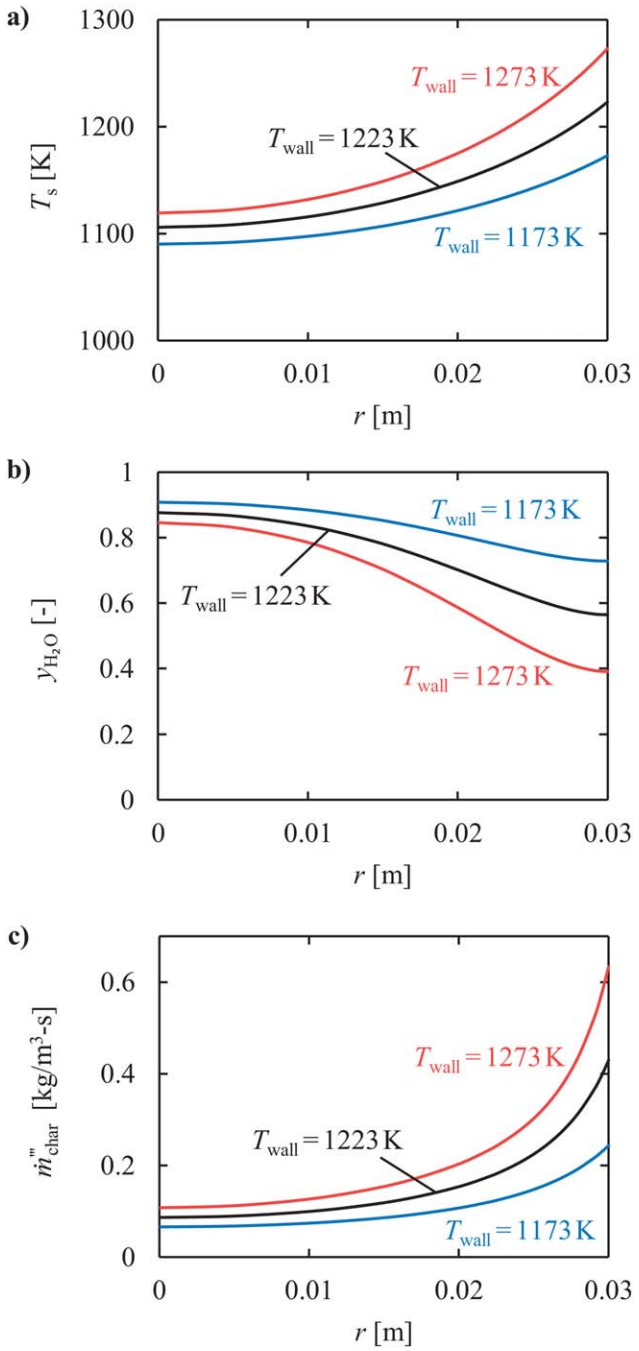

Figure 9. Simulated radial profiles of (a) solid temperature, (b) steam mole fraction, and (c) gasification rate at z = 0.5 m for l = 0.2 and T_{wall} = 1173, 1223, and 1273 K.

[Color figure can be viewed in the online issue, which is available at wileyonlinelibrary.com.]

bed ($\dot{n}_{C,syngas,RPC}$) and solid centerline temperatures at the outlet ($T_{s,center,outlet}$) are presented in Table 4. As shown by this table, increasing the wall temperature from 1173 to 1273 K leads to more than doubled $\dot{n}_{C,syngas,RPC}$ at the corresponding change in $T_{s,center,outlet}$ of only ~40 K.

Figure 9 presents simulated radial profiles of temperature, steam mole fraction, and gasification rate at the midplane of the domain (z = 0.5 m) for T_{wall} = 1173, 1223, and 1273 K. As shown in Figure 9a, the solid temperature and its slope are highest at the tube wall and are seen to increase with an increase in wall temperature as expected. Conversely, the steam mole fraction, plotted in Figure 9b, is the highest in the tube center and decreases with an increase in wall temperature. These observations can be attributed to the exponential temperature dependence of the gasification rate and the slow radial dispersion of steam leading to the steep profiles of the gasification rate per unit volume ($\dot{m}'''_C$) with the highest rates near the wall, see Figure 9c.

Figure 10 shows the responses of the syngas production rate ($\dot{n}_{C,syngas,RPC}$) and the temperatures at the outlet to changes in the particle loading (l) and the RPC properties (pore diameter, solid thermal conductivity, and porosity) for three wall temperatures (T_{wall} = 1173, 1223, and 1273 K). The changes are reported with respect to the reference conditions discussed above. Based on the results summarized in Figure 10a, one could draw the following inferences relative to the responses of syngas production rate.

1. Increasing d_{nom} or k_s at fixed φ_{RPC} results in an increase in the effective thermal conductivity of the RPC (k_{eff}), and thus, an increase in the overall gasification rate. An increase in d_{nom} leads to an increase in the radiative contribution due to a decrease in the extinction coefficient, thus its effect is more pronounced at higher temperatures. Conversely, the changes in k_s have a larger influence at lower temperatures due to the larger contribution of the conduction heat transfer to the effective thermal conductivity of the structure.
2. An increase in the volume fraction of the RPC solid 1 − φ_{RPC} is reflected by an increase in k_{cond} (Eq. 25) but impaired radiative heat transfer due to a higher extinction of radiation. The increase in 1 − φ_{RPC} is thus less beneficial at higher temperatures.
3. Of all the investigated parameters, the particle loading has the largest effect: a 25% increase in the particle loading leads to an increase in the overall gasification rate by 6–11%. The increase is especially pronounced at lower temperatures where the temperatures and gasification rates are more uniform.

Figure 10b shows the responses of the temperatures at the outlet of the domain as the difference between wall and centerline temperatures $\Delta T_{s,outlet} = T_{s,oulet,wall} - T_{s,outlet,center}$. It can be observed that:

1. An increase in d_{nom}, k_s, or $1-\varphi_{RPC}$ results in a higher effective thermal conductivity and thus a decrease in $\Delta T_{s,outlet}$. As for the overall gasification rate (Figure 10a), the sensitivity of $\Delta T_{s,outlet}$ is lower to k_s and 1 − φ_{RPC} as the wall temperature increases. No wall-temperature dependence was observed for the sensitivity to d_{nom}.
2. An increase in the particle loading leads to an increase in $\Delta T_{s,outlet}$ due to the reduced effective thermal conductivity and the increased consumption of heat of the gasification reaction. The sensitivity is larger at lower wall temperatures as the increase of the gasification rate is higher and more heat is consumed.

Numerical comparison of the trickle bed to a MB

An alternative to the incorporation of a trickle bed into a drop tube for increasing the residence time of char would be to operate the gasifier as a MB comprising beech char particles only (l = 1) that decrease in size along the way. This decrease in the particle size would result in a decrease in the bed's thermal conductivity that would lead to lower carbon

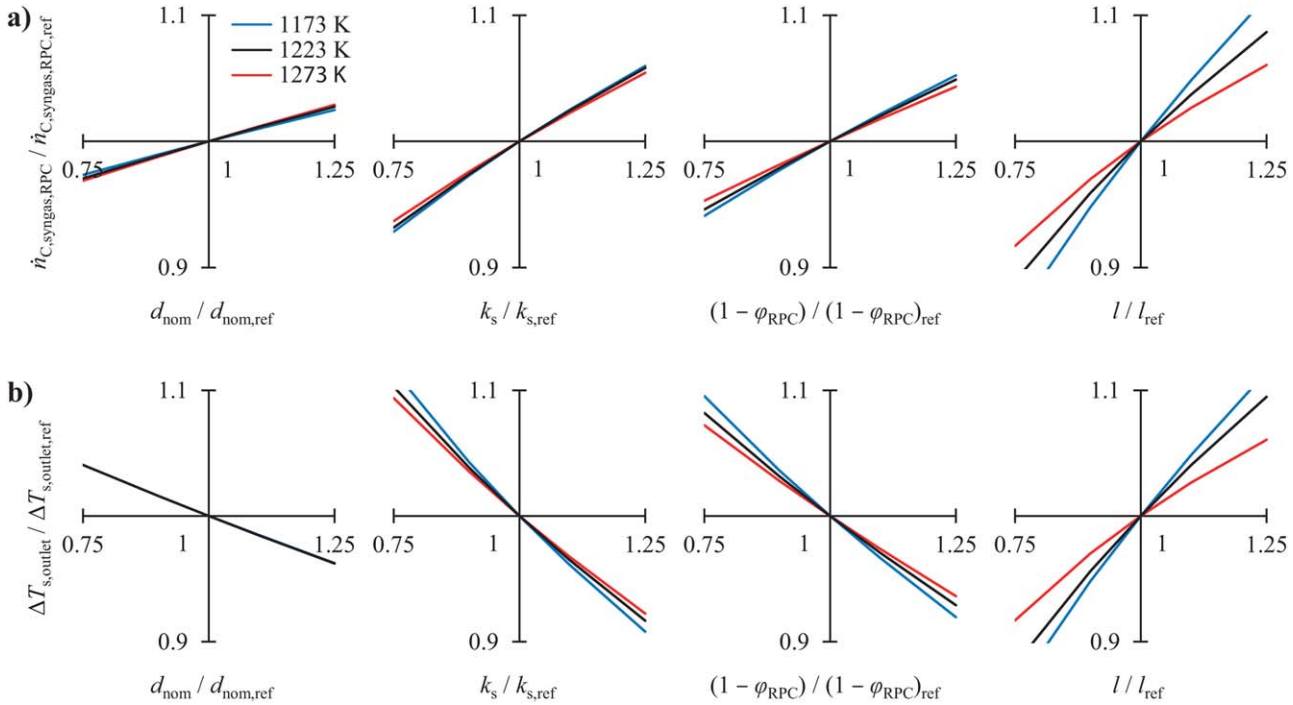

Figure 10. Sensitivity of (a) the syngas production rate ($\dot{n}_{C,syngas,RPC}$) and (b) the temperature difference between wall and centerline at the outlet of the domain $\Delta T_{s,outlet} = T_{s,oulet,wall} - T_{s,outlet,center}$ to changes in nominal pore diameter (d_{nom}), solid thermal conductivity (k_s), RPC porosity (φ_{RPC}), and particle loading (l) for T_{wall} = 1173, 1223, and 1273 K.

Reference case: d_{nom} = 2.54 mm, $k_s = k_{SiC}$, φ_{RPC} = 89%, and l = 0.2. [Color figure can be viewed in the online issue, which is available at wileyonlinelibrary.com.]

conversion rates. Our model, however, assumes that the MB retains its initial particle size (0.81 mm) and bed porosity ($\varphi_{MB} = 0.56$[20] throughout the reaction zone. By doing so, it estimates the highest carbon gasification rate the MB could deliver that can be then compared with its trickle-bed counterpart for the same flow rates, domain size, grid density, and boundary conditions specified in the previous section. Since the temperature differences between the solid and fluid phase are expected to be even smaller than in the RPC trickle-bed, the moving-bed model has been reduced to a pseudohomogeneous case, requiring only one energy equation to be solved. The pseudohomogeneous properties of the MB are calculated using the correlations listed in Table 5.[20,44–47] The effective thermal conductivity (k_{eff}) was based on a Yagi and Kunii model[47] with fitting parameters from Piatkowski.[20]

Figure 11 compares the MB and trickle bed (RPC) in terms of radial profiles of temperature, steam mole fraction, and gasification rate simulated for T_{wall} = 1223 K at z = 0.5 m. As compared to the MB, both the temperature and steam concentration profiles are more uniform across the RPC configurations operating at particle loadings l = 0.1–0.4, see Figures 11a, b. The steep temperature gradient in the MB close to the wall is also consistent with previously discussed effect of particle loading. The steam mole fraction at the wall decreases with an increase in the particle loading, thus, it is the lowest for the MB. At the centerline of the MB, the steam concentration does not differ considerably from the one at the inlet. Due to low core temperatures in the MB, the gasification rate, plotted in Figure 11c, approaches zero at about one third of the radius from the wall (~0.01 m) so the steam passes through unreacted. Conversely, the reaction within the RPC is more uniformly distributed and proceeds at a noticeable rate even in the center. The gasification rates in the regions closer to the wall increase with particle loading as more char is exposed to the highest temperatures. Therefore, the MB exhibited higher gasification rates at the wall then the trickle bed.

The higher core temperatures and reaction rates of the RPC configuration can be attributed to the heat-transfer enhancement brought in by the conduction through the RPC material and deeper penetration of radiation through the RPC pores. Figure 12 compares the effective thermal conductivities of the MB with N_2-filled voids and the RPC with different particle loadings. The presence of the RPC is seen to significantly increase the effective thermal conductivity of the domain. At lower temperatures and a particle loading of 0.4, a decrease in the effective thermal conductivity with increasing temperature is observed. This is due to a decrease of the conductivity of the RPC material (k_s). At lower particle loadings and higher temperatures the radiative contribution dominates resulting in a higher effective thermal conductivity.

Figure 13 compares the overall gasification rates at T_{wall} = 1173, 1223, and 1273 K calculated for the MB ($\dot{n}_{C,syngas,MB}$) and the trickle bed ($\dot{n}_{C,syngas,RPC}$) operating at various particle loadings (l). At low particle loadings, the

Table 5. Moving Bed Property Correlations

Quantity	Symbol	Source
Tortuosity	τ	Carman,[44] Appendix I
Dispersion coefficients	$D_{d,\perp}$; $D_{d,\parallel}$	Coelho and Guedes de Carvalho,[45] Eq. 17; Delgado,[46] Eq. 12
Bed effective thermal conductivity	k_{eff}	Piatkowski,[20] Yagi and Kunii[47]

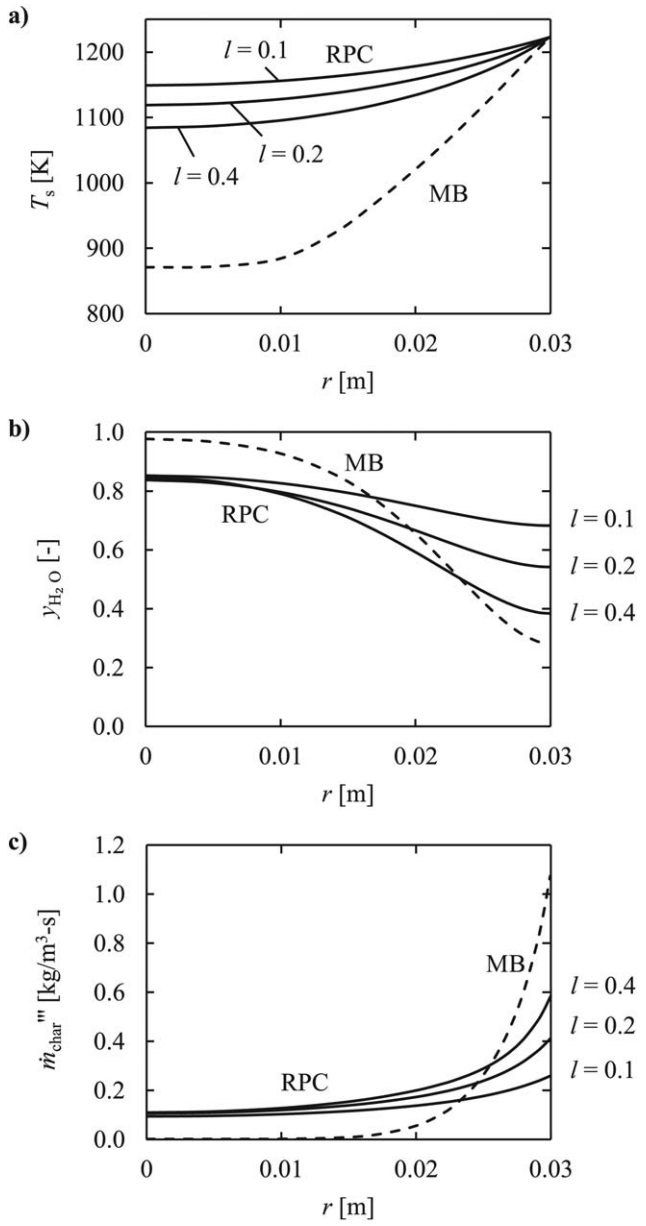

Figure 11. Simulated radial profiles of (a) solid temperature (T_s), (b) steam mole fraction (y_{H_2O}), and (c) gasification rate (m_C'') in moving bed (MB) and RPC (l = 0.1, 0.2, 0.4) at z = 0.5 m for T_{wall} = 1223 K.

overall gasification rate of the trickle bed is lower than in the MB, as less reacting material is present in the reactor. With an increase in the particle loading in the RPC, the ratio of trickle-bed to moving-bed gasification rates increases rapidly at first and then flattens. The steep increase at low particle loadings is almost linear with the particle loading. The flattening at higher particle loadings occurs due to the reduction in radiative contribution and reduced steam concentrations close to the wall. At wall temperatures of 1173 and 1273 K, the trickle bed outperforms the MB above particle loadings of 0.18 and 0.32, respectively. At T_{wall} = 1273 K, the trickle bed with l = 0.5 gasifies ~25% more carbon than the MB containing twice as much char.

Even though the gasification rates at low particle loadings are lower than in the MB, an RPC might be preferred as the higher core temperatures favor the decomposition of volatile

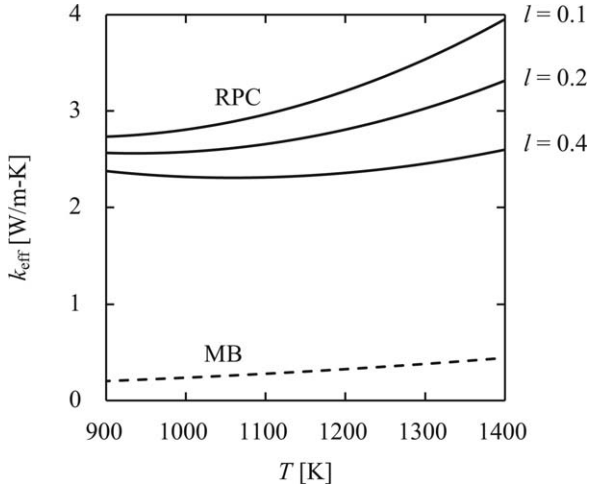

Figure 12. Effective thermal conductivity (k_{eff}) over temperature for the MB with N_2 filled voids and the RPC configuration at various loadings (l).

hydrocarbons passing through this zone, thereby improving the syngas quality. This is especially important when using feedstocks that release high amounts of hydrocarbons and tars.

Conclusions

A gas-solid trickle-bed reactor for the gasification of beech char particles was evaluated experimentally and numerically. Efficient delivery of externally supplied concentrated solar heat to the reaction site was achieved by incorporating a high conductivity RPC as packing into a drop-tube reactor that increased the residence time of the solids and enhanced the heat transfer to the gas phase. A series of 43–51 min gasification experiments in the temperature range 1173–1273 K with a mass flux of 6.5 g/s m^2 was conducted

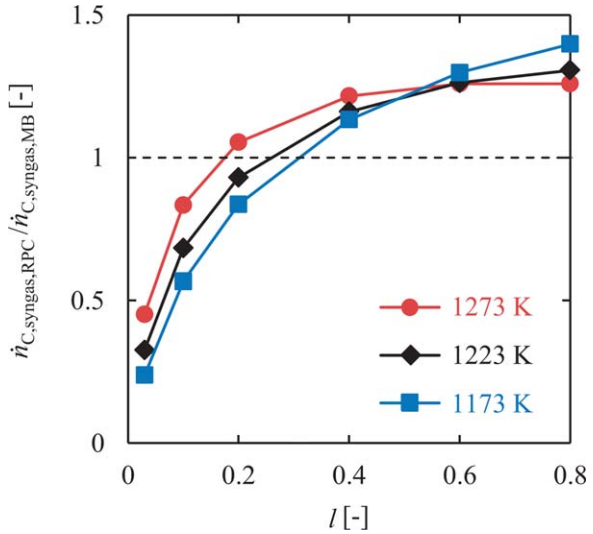

Figure 13. Simulation results for ratio of trickle-bed to moving-bed gasification rates as function of the particle loading in the RPC (l) and wall temperatures of T_{wall} = 1173, 1223, and 1273 K.

[Color figure can be viewed in the online issue, which is available at wileyonlinelibrary.com.]

with no pressure increase or clogging over the duration of the experiments. Compared to the drop-tube configuration, the carbon conversions attained under same conditions in the trickle-bed were significantly higher (<1% vs. 52%).

A 2-D finite-volume model of the trickle-bed reactor including chemical reaction coupled with conduction, convection, and radiation of heat within the porous structure was developed. Its predictions were in good agreement with measured reactor temperatures and gasification rates. A sensitivity analysis of the overall gasification rate and the core temperature, the key parameters for the capacity and gas phase selectivity, indicated that any effort to increase the effective thermal conductivity is beneficial. Reduced particle loadings increase the core temperatures but result in lower gasification rates.

A numerical comparison with a MB of char particles showed a more uniform temperature distribution over the cross-section of the trickle-bed. This is attributed to both high conductivity of the RPC and suppressed extinction of the radiation due to higher open porosity of the trickle-bed. The more uniform temperatures and thus the higher core temperatures are expected to improve gas-phase selectivity towards the desired product gas. Furthermore, it was shown that the gasification rates of the proposed configuration exceed those of a MB for particle loadings higher than 32% for a wall temperature of 1173 K and 18% for 1273 K, respectively.

Acknowledgments

Funding by the Brazilian-Swiss Joint Research Programme (Grant Agreement No. BJRP 011005) and by the European Union under the 7th Framework Program, Grant Nr. 609837 (STAGE-STE: Scientific and Technological Alliance for Guaranteeing the European Excellence in Concentrating Solar Thermal Energy) is gratefully acknowledged.

Notation

A_0 = specific surface area, m^2/m^3
d_{nom} = nominal pore diameter, m
d_{tube} = tube diameter, m
D = diffusion/dispersion coefficient, m^2/s
E_A = activation energy, kJ/mol
E = error, corresponding units
e_s = sensible energy, J/m^3
F = configuration factor, -
h_{sf} = interfacial heat-transfer coefficient, W/m^2 K
ΔH_R = reaction enthalpy, J/mol
k = thermal conductivity, W/m K
k_0 = frequency factor in Eq. 12, 1/s bar
k_0'' = frequency factor in Eq. 13, mol/m^2 s bar
K = extinction coefficient, 1/m
l = particle loading, -
m = mass, kg
$\dot{m}$ = mass flow rate, kg/s
$\dot{m}_C'''$ = mass consumption rate of carbon per unit volume, kg/m^3 s
M = molar mass, kg/mol
M = Mach number, -
$\dot{n}$ = molar flow rate, mol/s
N = number of species, -
N_{surf} = number of surfaces, -
N_C = number of moles of carbon, mol
p = pressure / partial pressure, bar
Pe = Péclet number, -
$\dot{Q}$ = heat-transfer rate, W
q = heat flux, W/m^2
q_a = order of accuracy, -
R = residual / gas constant, -/ 8.3145, J/mol-K
r = radial coordinate, m
r_C = carbon gasification rate per mole of carbon, 1/s = mol/mol s
r_C'' = carbon gasification rate per surface area of char, mol/m^2 s
Re = Reynolds number, -
S_k = mass source of species k, kg/m^3 s
S_C = surface area of char particle, m^2
T = temperature, K
u = fluid superficial velocity, m/s
V = volume, m^3
v^C = correction velocity, m/s
w_k = mass fraction of species k in fluid, -
x = elemental molar ratio of H/C in feedstock, -
x_i = mass fraction of species i in solid, -
X_C = carbon conversion, -
y = elemental molar ratio of O/C in feedstock, -
y_k = mole fraction of species k in fluid, -
z = axial coordinate, m

Greek letters

γ = heat capacity ratio, -
ε = emissivity, -
κ = optical thickness, -
μ = dynamic viscosity, Pa s
ρ = density, kg/m^3
σ = Stefan–Boltzmann constant $5.67 \cdot 10^{-8}$, W/m^2 K^4
φ = porosity, -

Subscripts

$\parallel$ = parallel to main flow direction
$\perp$ = perpendicular to main flow direction
cond = conduction
eff = effective
exp = experiment
f = fluid
k = species index
rad = radiation
s = solid
sim = numerical simulation
0 = initial

Abbreviations

LHV = lower heating value
ppi = pores per inch
RPC = reticulate porous ceramic

Literature Cited

1. Taylor RW, Berjoan R, Coutures JP. Solar gasification of carbonaceous materials. *Sol Energy*. 1983;30(6):513–525.
2. Piatkowski N, Wieckert C, Weimer A, Steinfeld A. Solar-driven gasification of carbonaceous feedstock—a review. *Energy Environ. Sci.* 2010;4:73–82.
3. Lichty P, Perkins C, Woodruff B, Bingham C, Weimer A. Rapid high temperature solar thermal biomass gasification in a prototype cavity reactor. *J Solar Energy Eng*. 2010;132(1):0110121–0110127.
4. Melchior T, Steinfeld A. Radiative transfer within a cylindrical cavity with diffusely/specularly reflecting inner walls containing an array of tubular absorbers. *J Solar Energy Eng*. 2008;130(2): 0210131–0210137.
5. Weimer AW, Perkins C, Mejic D, Lichty P. High temperature pyrolysis or gasification to carbon monoxide and hydrogen using solar energy; heating in entrainment reactor; carbothermic reduction of metal oxide particles by biomass pyrolysis products; reaction with steam to produce hydrogen. U.S. Patent 8,287,610, 2012.
6. Perkins C, Jovanovic Z, Strand S, Kelley D, Minden A, Ridley R. Systems and methods for biomass gasifier reactor and receiver configuration. U.S. Patent 8,821,599, 2014.
7. Jovanovic Z, Schramm B, Perkins C, Hilton C, Simmons W. Systems and methods for biomass grinding and feeding. U.S. Pat. Appl. 2010/0242353, 2010.
8. Melchior T, Perkins C, Lichty P, Weimer AW, Steinfeld A. Solar-driven biochar gasification in a particle-flow reactor. *Chem Eng Process Process Intensification*. 2009;48(8):1279–1287.

9. Melchior T, Perkins C, Weimer AW, Steinfeld A. A cavity-receiver containing a tubular absorber for high-temperature thermochemical processing using concentrated solar energy. *Int J Therm Sci*. 2008; 47(11):1496–1503.
10. Klein HH, Rubin R, Karni J. Experimental evaluation of particle consumption in a particle seeded solar receiver. *J Solar Energy Eng*. 2007;130(1):011012–011012.
11. Piatkowski N, Steinfeld A. Solar-driven coal gasification in a thermally irradiated packed-bed reactor. *Energy Fuels*. 2008;22(3):2043–2052.
12. Piatkowski N, Wieckert C, Steinfeld A. Experimental investigation of a packed-bed solar reactor for the steam-gasification of carbonaceous feedstocks. *Fuel Process Technol*. 2009;90(3):360–366.
13. Barysheva LV, Borisova ES, Khanaev VM, Zolotarskii IA, Pakhomov NA, Noskov AS. Motion of particles through the fixed bed in a gas–solid–solid downflow reactor. *Chem Eng J*. 2003;91(2–3):219–225.
14. Roes AWM, Van Swaaij WPM. Hydrodynamic behaviour of a gas–solid counter-current packed column at trickle flow. *Chem Eng J*. 1979;17(2):81–89.
15. Saatdjian E, Large JF. Heat transfer simulation in a raining packed bed exchanger. *Chem Eng Sci*. 1985;40(5):693–697.
16. Westerterp KR, Kuczynski M. Gas-solid trickle flow hydrodynamics in a packed column. *Chem Eng Sci*. 1987;42(7):1539–1551.
17. Kiel JHA, Prins W, Van Swaaij WPM. Modelling of non-catalytic reactions in a gas-solid trickle flow reactor: dry, regenerative flue gas desulphurisation using a silica-supported copper oxide sorbent. *Chem Eng Sci*. 1992;47(17–18):4271–4286.
18. Verver AB, Vanswaaij WPM. The heat-transfer performance of gas solid trickle flow over a regularly stacked packing. *Powder Technol*. 1986;45(2):133–144.
19. Kruesi M, Jovanovic ZR, Steinfeld A. A two-zone solar-driven gasifier concept: reactor design and experimental evaluation with bagasse particles. *Fuel*. 2014;117, Part A:680–687.
20. Piatkowski N. *Solar Driven Steam Gasification of Carbonaceous Feedstocks: Feedstock Characterization to Pilot Facility Testing*, ETH Zurich, 2011.
21. Hobbs ML, Radulovic PT, Smoot LD. Modeling fixed-bed coal gasifiers. *AIChE J*. 1992;38(5):681–702.
22. Toscano G, Corinaldesi F. Ash fusibility characteristics of some biomass feedstocks and examination of the effects of inorganic additives. *J Agric Eng*. 2010;41(2):13–19.
23. Weimer AW, Clough DE. Modeling of char particle size/conversion distributions in a fluidized bed gasifier: non-isothermal effects. *Powder Technol*. 1980;27(1):85–103.
24. Poinsot T, Veynante D. *Theoretical and Numerical Combustion*, 2nd ed. Philadelphia: Edwards, 2005.
25. Siegel R, Howell JR. *Thermal Radiation Heat Transfer*, 4th ed. New York: Taylor & Francis, 2002.
26. Kruesi M, Jovanovic ZR, dos Santos EC, Yoon HC, Steinfeld A. Solar-driven steam-based gasification of sugarcane bagasse in a combined drop-tube and fixed-bed reactor—thermodynamic, kinetic, and experimental analyses. *Biomass Bioenergy*. 2013;52:173–183.
27. Moilanen A, Saviharju K, Harju T. Steam gasification reactivities of various fuel chars. In: Bridgwater AV, editor. *Advances in Thermochemical Biomass Conversion*. Springer: Netherlands, 1993:131–141.
28. Leuenberger RH, Person RA. Compilation of Radiation Shape Factors for Cylindrical Assemblies. *ASME paper 56-A-144, ASME Annual Meeting*. New York 1956.
29. Buschman AJ, Pittman CM. Configuration factors for exchange of radiant energy between axisymmetrical sections of cylinders, cones and hemispheres and their bases. *NASA TN D-944*. 1961.
30. Touloukian YS, DeWitt DP. *Thermal Radiative Properties: Nonmetallic Solids*. New York: IFI/Plenum, 1972.
31. Siegel R. Transient radiative cooling of a droplet-filled layer. *J Heat Transf*. 1987;109(1):159–164.
32. Petrasch J. *Multi-Scale Analyses of Reactive Flow in Porous Media*, ETH Zurich, 2007.
33. Suter S, Haussener S. Morphology Engineering of porous media for enhanced solar fuel and power production. *Jom*. 2013:1–8.
34. Fuller EN, Schettle. Pd, Giddings JC. A new method for prediction of binary gas-phase diffusion coeffecients. *Ind Eng Chem*. 1966; 58(5):19–27.
35. Fairbanks DF, Wilke CR. Diffusion coefficients in multicomponent gas mixtures. *Ind Eng Chem*. 1950;42(3):471–475.
36. Munro RG. Material properties of a sintered alpha-SiC. *J Phys Chem Ref Data*. 1997;26(5):1195–1203.
37. Yaws CL. *Transport Properties of Chemicals and Hydrocarbons: Viscosity, Thermal Conductivity, and Diffusivity for more than 7800 Hydrocarbons and Chemicals, Including C1 to C100 Organics and Ac to Zr Inorganics*: Norwich, NY: Elsevier Science, 2009.
38. Chase MW, National Institute of Standards and Technology (U.S.). *NIST-JANAF Thermochemical Tables*, 4th ed. Washington, DC: American Chemical Society; New York: American Institute of Physics for the National Institute of Standards and Technology; 1998.
39. Merrick D. Mathematical-models of the thermal-decomposition of coal .2. Specific-heats and heats of reaction. *Fuel*. 1983;62(5):540–546.
40. Spalding DB. A novel finite difference formulation for differential expressions involving both first and second derivatives. *Int J Numer Methods Eng*. 1972;4(4):551–559.
41. Davis TA. Algorithm 832: UMFPACK V4.3 – an unsymmetric-pattern multifrontal method. *ACM Trans Math Softw*. 2004;30(2): 196–199.
42. Roache PJ. Code verification by the method of manufactured solutions. *J Fluid Eng*. 2002;124(1):4–10.
43. Knupp P, Salari K. *Verification of Computer Codes in Computational Science and Engineering*, Boca Raton, FL: Chapman and Hall/CRC, 2003.
44. Carman PC. Fluid flow through granular beds. *Trans Inst Chem Eng*. 1937;15:150–166.
45. Coelho MAN, Guedes de Carvalho JRF. Transverse dispersion in granular beds. I: Mass transfer from a wall and the dispersion coefficient in packed beds. *Chem Eng Res Des*. 1988;66(2):165–177.
46. Delgado JMPQ. A critical review of dispersion in packed beds. *Heat Mass Transf*. 2006;42(4):279–310.
47. Yagi S, Kunii D. Studies on effective thermal conductivities in packed beds. *AIChE J*. 1957;3(3):373–381.

Manuscript received July 14, 2014, and revision received Oct. 7, 2014.